NANO LETTERS

pubs.acs.org/NanoLett

Letter

Heat Conductor–Insulator Transition in Electrochemically Controlled Hybrid Superlattices

Jiawei Zhou,[#] Yecun Wu,[#] Heungdong Kwon, Yanbin Li, Xin Xiao, Yusheng Ye, Yinxing Ma, Kenneth E. Goodson, Harold Y. Hwang,* and Yi Cui*

Cite This: *Nano Lett.* 2022, 22, 5443–5450

Read Online

ACCESS | Metrics & More | Article Recommendations | Supporting Information

ABSTRACT: Designing materials with ultralow thermal conductivity has broad technological impact, from thermal protection to energy harvesting. Low thermal conductivity is commonly observed in anharmonic and strongly disordered materials, yet a microscopic understanding of the correlation to atomic motion is often lacking. Here we report that molecular insertion into an existing two-dimensional layered lattice structure creates a hybrid superlattice with extremely low thermal conductivity. Vibrational characterization and *ab initio* molecular dynamics simulations reveal strong damping of transverse acoustic waves and significant softening of longitudinal vibrations. Together with spectral correlation analysis, we demonstrate that the molecular insertion creates liquid-like atomic motion in the existing lattice framework, causing a large suppression of heat conduction. The hybrid materials can be transformed into solution-processable coatings and used for thermal protection in wearable electronics. Our work provides a generic mechanism for the design of heat insulators and may further facilitate the engineering of heat conduction based on understanding atomic correlations.

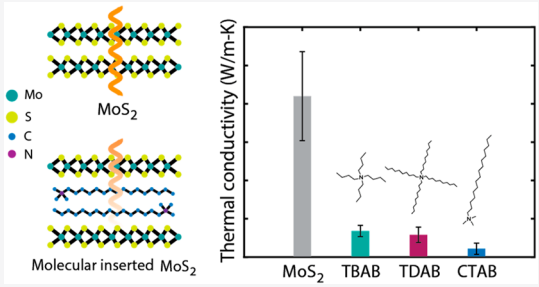

KEYWORDS: *Layered materials, Electrochemical intercalation, Thermal conductivity, Atomic vibrations*

Heat transport in solids is governed by its thermal conductivity, which spans over 5 orders of magnitude at room temperature. Designing materials toward the upper or lower extremes has an impact over a broad range of technologies,[1] from thermal barrier coatings in turbine blades to substrates in electronic devices.[2] Significant progress has been made in recent years in the discovery and synthesis of superior heat conductors.[3−8] Band structure engineering of phonons, which are collective atomic vibrations that carry heat, and isotope enrichment are shown to be effective strategies toward high lattice thermal conductivity, with room-temperature values of over 1000 W/m·K achieved in boron arsenide[5−7] and cubic boron nitride.[8] At the other end, materials with low thermal conductivity are important for thermal protection and thermoelectric energy conversion. Exploring general mechanisms that strongly suppress phonon transport has great potential to expand the materials toolbox for heat insulators.

The thermal conductivity of insulating crystalline solids is mostly dominated by phonons, which involve coherent atomic motions in the lattice and propagate as waves.[9] A common strategy for impeding phonon propagation is to introduce defects, such as atomic impurities, grain boundaries,[10] stacking disorder,[11] and so forth. These defects generally increase elastic phonon scattering, leading to shorter phonon mean free paths and lower thermal conductivity.[12] When the disorder is sufficiently strong, phase-preserving phonon-defect scatterings can lead to Anderson localization of phonons and can strongly suppress heat conduction.[13] A contrasting approach is to increase inelastic phonon scattering by designing atomic lattices with strong phonon anharmonicity,[14,15] breaking phonon coherence. Such lattice structures often host intrinsically soft components supported by rigid frameworks, as found in organic/inorganic perovskites[16,17] and superionic conductors.[18] While the soft sublattice can exhibit liquid-like atomic motions and associated low thermal conductivity,[19] the rigid framework limits the extent to which the heat transport can be suppressed. Breaking the vibrational coherence of an existing framework at the entire lattice structure level would allow for much greater suppression in heat transport.

Intercalation in layered materials presents an opportunity to control the vibrational coupling between different planes across the entire layered structure.[20] Changes in thermal conductivity have been previously observed in ionically intercalated layered materials,[21−23] yet the contrast in thermal conductivity is usually within a factor of five because the structure remains as a solid framework. We hypothesize that the interlayer vibrational

Received: April 14, 2022
Revised: June 15, 2022
Published: June 17, 2022

https://doi.org/10.1021/acs.nanolett.2c01407
Nano Lett. 2022, 22, 5443−5450

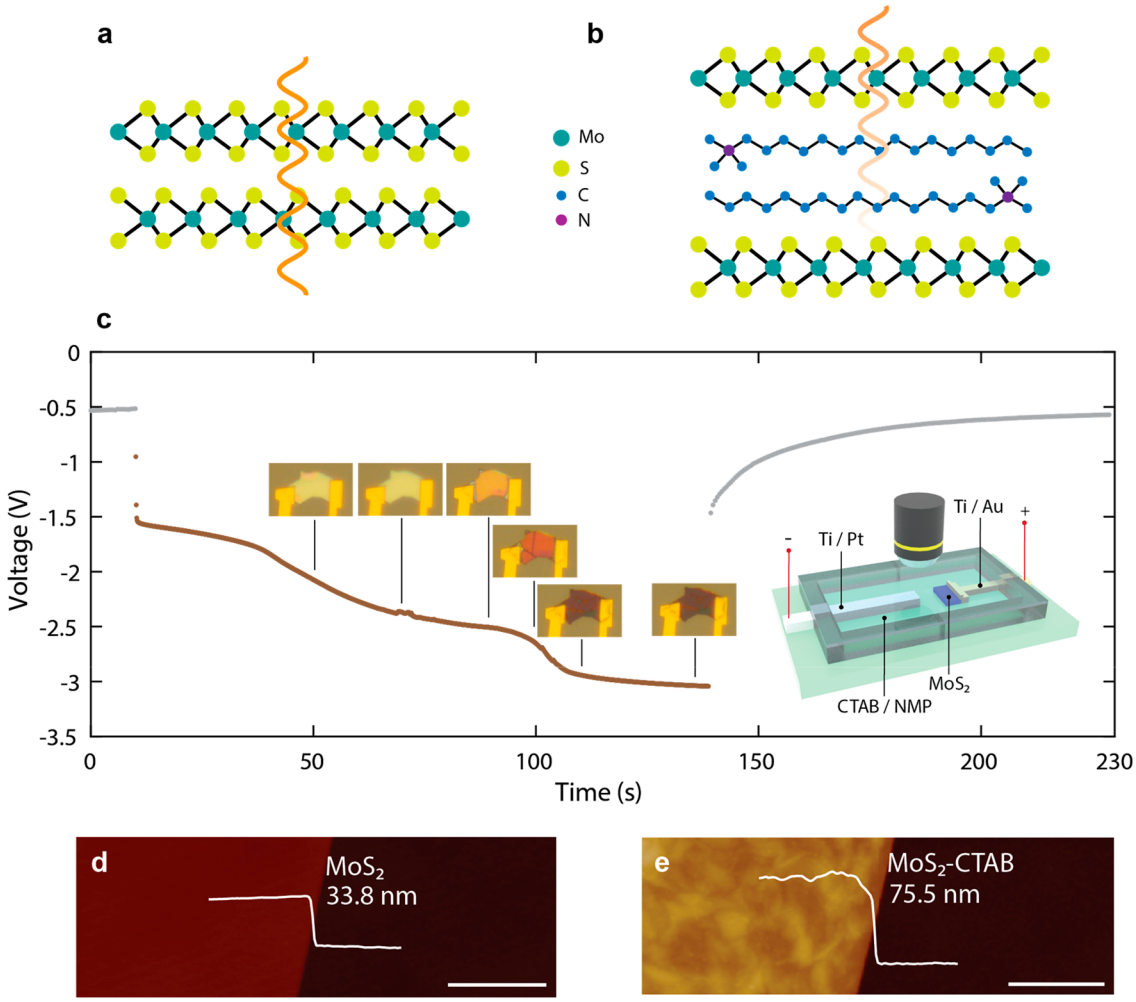

Figure 1. Molecular hybrid superlattice structure. (a) Conventional superlattice structure, where heat-carrying vibrational modes propagate through the lattice. (b) Hybrid superlattice structure with a soft molecular interlayer, for which heat-carrying waves are strongly damped. Hydrogen atoms are not drawn in the schematic. (c) *In situ* electrochemical intercalation showing the process of molecular insertion into the MoS_2 lattice. AFM images of (d) an MoS_2 flake and (e) the flake after CTAB intercalation. Scale bar: 1 μm.

coherence in an inorganic crystal/molecule hybrid heterostructure would be broken, leading to a large reduction in thermal conductivity. Using MoS_2 as the crystalline framework, we demonstrate that molecular insertion can lead to a very large drop in the cross-plane thermal conductivity, reduced by a factor of >20 at room temperature. Compared to bulk MoS_2, the minimum thermal conductivity achieved in molecularly intercalated MoS_2 has a thermal conductivity that is nearly 2 orders of magnitude smaller (about 0.06 W/m-K, only twice that of air). Vibrational spectroscopy and *ab initio* molecular dynamics further demonstrate how interlayer vibrational coherence is lost through molecular insertions, providing a general route for designing extremely heat-insulating materials.

We choose to study 2H-MoS_2 because of its simple lattice. 2H-MoS_2 has a layered structure with a hexagonal unit cell. Despite the weak van der Waals interlayer interaction, the cross-plane thermal conductivity of naturally occurring MoS_2 is about 3−5 W/m·K at room temperature, which is comparable to even those of some metal alloys and semimetals (e.g., steel and bismuth). This is because the ordered lattice structure supports long-wavelength phonons that can propagate through the layers[24] (Figure 1a). As a result, its thermal conductivity decreases with temperature in the high-temperature regime, a trend commonly observed in crystalline materials. The insertion of molecules into the interlayer space creates two major changes (Figure 1b). First, highly anharmonic molecular vibrations tend to decouple the MoS_2 planes, breaking their vibrational coherence. Second, for those phonons that remain coherent, the intrinsic disorder of the molecular packing creates strong phonon damping and thereby impedes their propagation. We therefore expect the thermal transport in all channels to be strongly suppressed.

The insertion of molecules into MoS_2 is carried out by electrochemical intercalation.[25] To visualize the intercalation process, an optical cell is fabricated (Figure S1). Prepatterned 5/50 nm Ti/Pt is used as the counter electrode, and exfoliated MoS_2 flakes (50−90 nm) with a Ti/Au contact serve as the working electrode. The entire system with electrolyte is sealed by a thermoplastic film and a transparent glass coverslip cover for *in situ* observation. An organic solvent containing cationic molecules (∼5 mg/mL) is used as the electrolyte. Figure 1c shows the example of the intercalation of cetyltrimethylammonium bromide (CTAB, $C_{16}H_{33}N(CH_3)_3Br$). At about −2.4 V, we start to observe the intercalation of molecules into MoS_2. The intercalation occurs from the sides of the flakes and through different stages, accompanied by color changes. (The

https://doi.org/10.1021/acs.nanolett.2c01407
Nano Lett. 2022, 22, 5443−5450

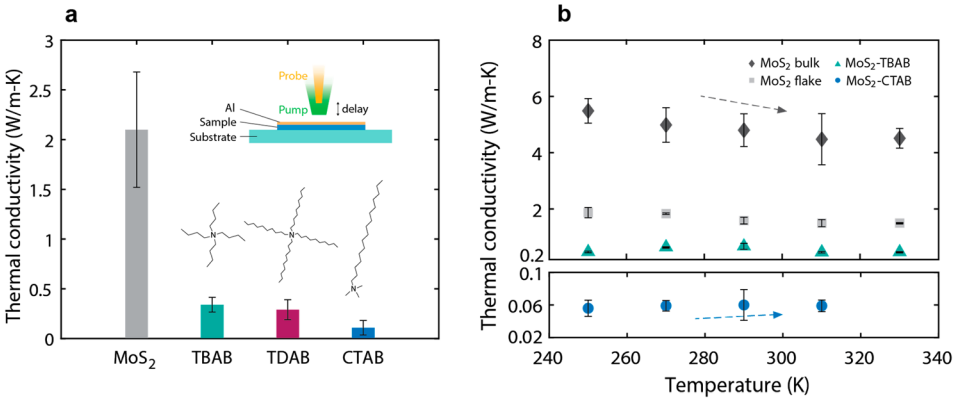

Figure 2. Thermal conductivity of molecularly inserted MoS_2. (a) Thermal conductivity of pristine MoS_2 flakes and molecularly intercalated MoS_2 at room temperature. The pristine MoS_2 flakes have thicknesses of around 50−90 nm. The error bars represent one standard deviation of the averaged thermal conductivity of measurement on at least three different samples. (b) Temperature-dependent thermal conductivity of MoS_2 and intercalated samples. For CTAB-intercalated MoS_2, the highest temperature measurements are limited to 310 K to avoid potential material degradation. The error bars represent one standard deviation of the averaged thermal conductivity of three measurements on the same sample.

full intercalation process can be found in Supporting Information Movie 1.) The intercalation stops at a voltage slightly below −3 V. Atomic force microscope (AFM) studies show that, compared to pristine MoS_2, the thickness of CTAB-intercalated MoS_2 is increased by about 130% (Figure 1d,e), consistent with an X-ray diffraction (XRD) measurement showing an increase in the interlayer distance from 6.15 Å in pristine MoS_2 to about 15 Å in CTAB-intercalated MoS_2 (Figure S2).

The thermal conductivities of pristine and molecularly inserted MoS_2 are measured with a pump−probe optical method based on time-domain thermoreflectance (TDTR) signals.[26,27] (See details in the Supporting Information and representative TDTR signals in Figure S3.) We note that for samples with ∼100 nm thickness and relatively low thermal conductivity, the TDTR signals are mostly sensitive to the thermal conductivity of the sample and not to the substrate properties (Figure S4). Moreover, because the TDTR-based thermal conductivity measurement is affected by the heat capacity used in the fitting process, heat capacities are determined either from direct temperature-dependent measurements of molecularly inserted samples or from indirect estimation based on separate heat capacity measurements of MoS_2 crystals and molecules. (See the discussions in the Supporting Information.) We also note that the TDTR sensitivity to the heat capacity is generally smaller than the sensitivity to the thermal conductivity (Figure S4). Pristine MoS_2 flakes have a thermal conductivity slightly lower than that of bulk MoS_2 because of the boundary scattering that suppresses the heat conduction of phonons with mean free paths larger than the flake thickness.[28] After MoS_2 is intercalated with molecules, we observe a significant reduction in the thermal conductivity (Figure 2a), accompanied by a large expansion in the interlayer spacing (Figure S2). Various molecules have been studied. Among them, tetradecylammonia bromide (TDAB, $(C_{10}H_{21})_4NBr$) has the largest interlayer spacing expansion (from 6.15 to about 24.6 Å). Tetrabutylammonia bromide (TBAB, $(C_4H_9)_4NBr$) shows modest increases in interlayer spacing (to about 19.2 Å), and CTAB shows the smallest change (to about 15 Å). On the basis of the thickness change and the molecule type, TBAB molecules are likely to possess a vertical configuration in the interlayer space and CTAB molecules more likely reside as horizontal bilayers. (See the discussions in the Supporting Information.) Even though the interlayer spacing change in CTAB is not as large as in TDAB, the thermal conductivity measured in the MoS_2-CTAB sample is the lowest, about half of that when TDAB is inserted, and nearly a factor of 20 smaller than intrinsic MoS_2 flakes. This makes CTAB-inserted MoS_2 among the best heat insulators at room temperature. We note that heat insulators with similar inorganic/organic hybrid structure have been previously reported in organoclay nanolaminates through self-assembly synthesis,[29] where the thermal conductivity reduction compared to unmodified clay is about a factor of 5. The extremely low thermal conductivity in CTAB-inserted MoS_2 may benefit from the horizontal configuration of CTAB molecules, whereas the possible vertical or tilted alignment of TBAB and TDAB molecules in the interlayer space could instead facilitate the interlayer vibrational coupling.

Accompanying the large reduction in thermal conductivity is a change in the temperature dependence of thermal conductivity, indicating possible shifts in the thermal transport regime (Figure 2b). Bulk and thin MoS_2 share similar temperature-dependent thermal conductivities—both decrease with temperature, an effect commonly attributed to increased phonon−phonon scattering at higher temperatures in crystalline materials. TBAB-inserted MoS_2 exhibits an initially increasing thermal conductivity and then a decreasing trend, a behavior resembling that of polycrystalline materials.[30] For polycrystalline structures, the mean free paths at lower temperatures are limited by the grain size, and the thermal conductivity increases with temperature as more phonon modes are populated. At higher temperatures, when the phonon−phonon scatterings are strong, the intrinsic phonon−phonon mean free paths become smaller than the grain size and decrease with temperature, leading to decreasing thermal conductivity. While molecularly inserted MoS_2 is not a polycrystalline material, the random molecular packing between layers creates stacking disorder that serves as effective two-dimensional defects which impede phonon transport in the cross-plane direction, similar to polycrystalline structures. Most intriguingly, CTAB-inserted MoS_2 shows a qualitatively different trend—its thermal conductivity slightly increases with temperature and nearly saturates above room temperature. Such a trend is usually observed in highly disordered systems, such as amorphous materials.[31] The temperature dependence

https://doi.org/10.1021/acs.nanolett.2c01407
Nano Lett. 2022, 22, 5443−5450

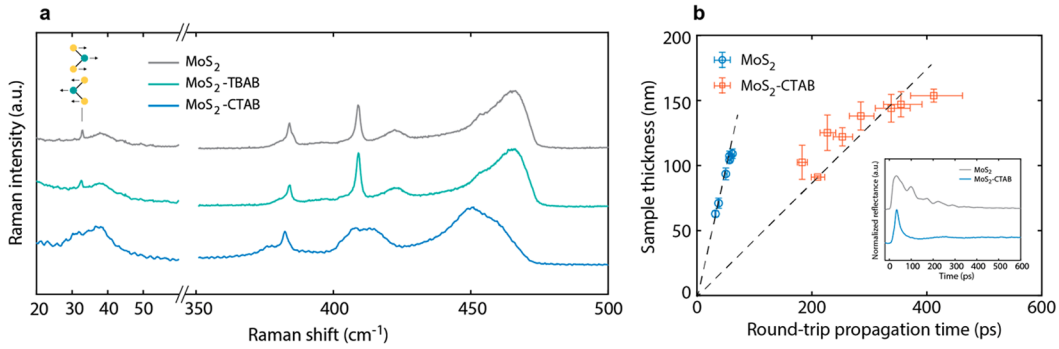

Figure 3. Raman and acoustic characterization. (a) Raman spectra of MoS_2 and molecularly intercalated MoS_2, spanning both low-frequency and midfrequency regions. The low-frequency peak is due to the interlayer shear mode. (b) Round-trip propagation time with respect to sample thickness in MoS_2 and CTAB-intercalated MoS_2 from picosecond acoustic measurements. The inset shows representative picosecond acoustic data (normalized amplitude signals) which displays the launch and propagation of longitudinal acoustic waves across the samples. The dashed line results from a linear fit to the data.

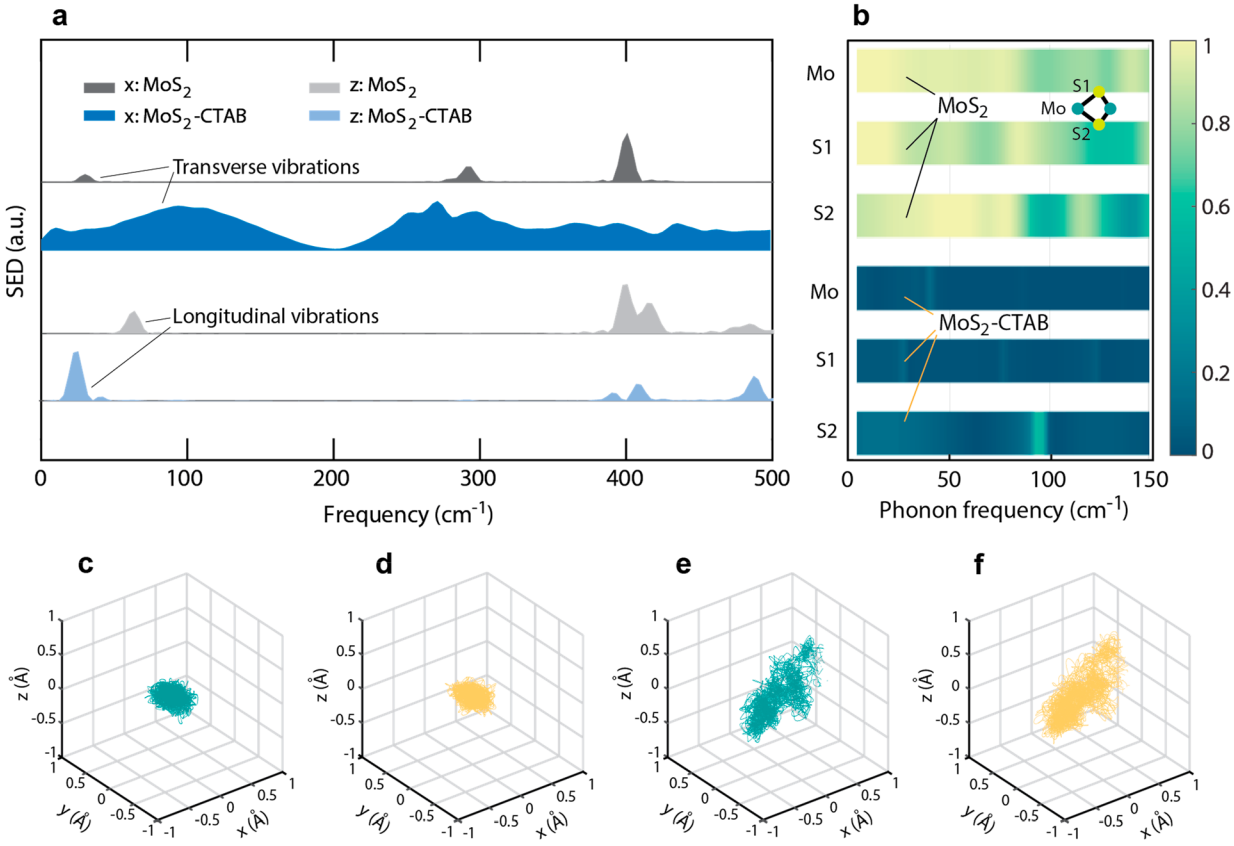

Figure 4. *Ab initio* atomic dynamics. (a) Calculated spectral energy density from an *ab initio* molecular dynamics simulation for $\mathbf{q} = 0$ in the transverse and longitudinal directions. Strong damping of transverse vibrations and a significant softening of the low-frequency longitudinal vibration are observed. (b) Normalized cross-spectral energy density between atoms located in different MoS_2 planes separated by the interlayer space in the color plot. The Mo, S1, and S2 atoms indicate the first atom of the atomic pairs and are the three atoms within the same MoS_2 hexagonal unit cell. Simulated atomic trajectories of (c) Mo and (d) S atoms in pristine MoS_2. Simulated atomic trajectories of (e) Mo and (f) S atoms in CTAB-intercalated MoS_2.

of the thermal conductivity together with the extremely low thermal conductivity indicates that the vibrational modes that carry the dominant heat are likely undergoing fundamental changes.[32]

Molecular packing in layered structures can take various geometries because of the high configurational degrees of freedom. Furthermore, the hydrogen atom in the alkyl chain is highly anharmonic.[33] These two effects together decouple the vibrational coherence between the MoS_2 planes. To illustrate how vibrational modes in MoS_2 are altered by molecular insertion, we recorded low-frequency Raman spectra (Figure 3a). Pristine MoS_2 possesses an interlayer shearing mode at ~32 cm^{-1}, for which adjacent MoS_2 layers vibrate against each other coherently in the horizontal direction.[34] This shearing mode is observable in TBAB-inserted samples but is hardly discernible in CTAB-inserted ones. This suggests that the

https://doi.org/10.1021/acs.nanolett.2c01407
Nano Lett. 2022, 22, 5443−5450

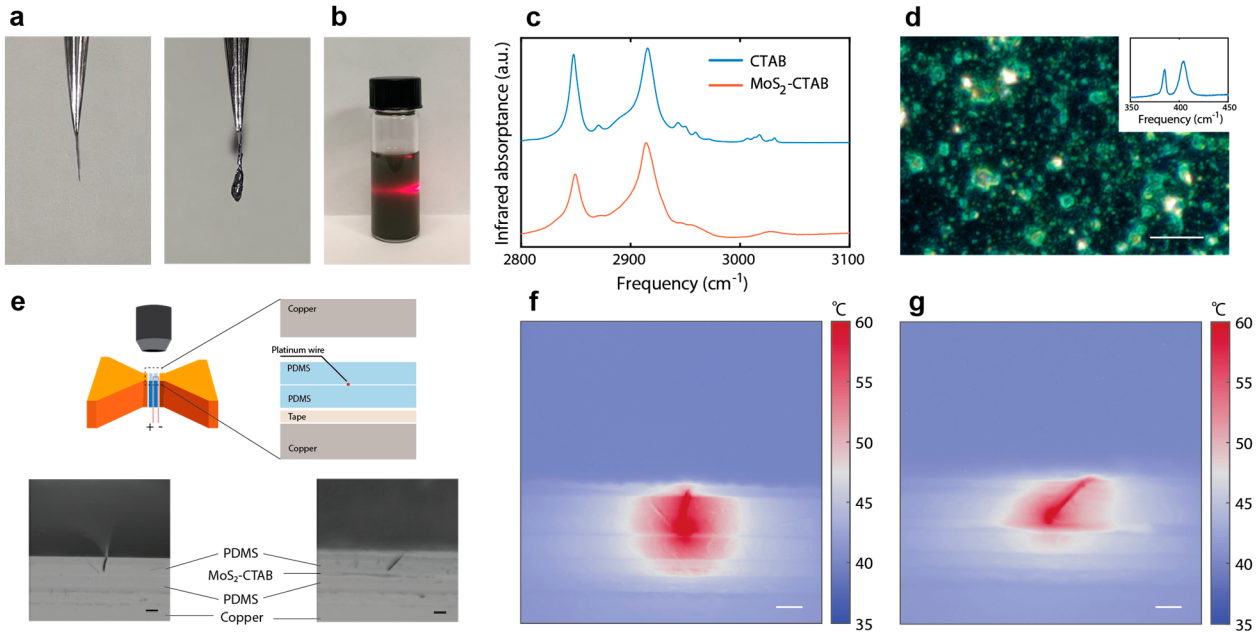

Figure 5. Solution processing and infrared imaging of thermal isolation materials. (a) Pictures showing an MoS_2 crystal before intercalation (left) and after intercalation (right). (b) Molecularly intercalated MoS_2 flakes suspended in dimethylformamide. (c) ATR-FTIR spectrum of CTAB molecules and dried CTAB-intercalated MoS_2 materials from 2800 to 3100 cm^{-1}, showing C−H vibrations. (d) Dark-field microscope image showing MoS_2 flakes after solution coating. The scale bar is 10 μm. The inset shows the corresponding Raman spectra. (e) Schematic showing the infrared temperature imaging setup and the cross-section of the device used to visualize heat spreading with a local hot spot. The PDMS is taped to one copper plate. Images on the bottom show pictures without (left panel) and with (right panel) the thermal isolation material (CTAB-intercalated MoS_2). The scale bar is 200 μm. Infrared microscopic temperature mapping of heat spreading on soft substrates, (f) without and (g) with the thermal isolation material. The temperature is shown as a color map. Scale bar: 200 μm.

shearing mode and thus the transverse vibrations that couple MoS_2 in different planes are strongly damped in the latter case. Mid-frequency-range Raman spectra also reveal a significant change in the spectral feature at around 420−430 cm^{-1} (Figure 3a). This dispersive feature has been attributed to two-phonon Raman processes that involve longitudinal and transverse acoustic phonons at the zone boundary.[35] After molecular insertion, this dispersive feature undergoes a large red shift, indicating that the acoustic phonons may be significantly softened.

While the shearing mode is strongly suppressed and may no longer be well-defined, we suspect that longitudinal phonons with predominantly vertical displacements still exist, but with reduced group velocities. To reveal the impact of molecular insertion on longitudinal phonons, we use picosecond acoustic measurements to launch acoustic pulses and monitor their propagation (inset of Figure 3b). As the acoustic pulses are generated by thermal expansion due to transient heating of the pump pulse, longitudinal waves are mostly excited. Compared to pristine MoS_2, where acoustic oscillations with shorter periods can be observed, much broader oscillation cycles are observed in CTAB-inserted MoS_2. These oscillations correspond to the round-trip propagation of longitudinal acoustic waves across the sample thickness. (See the representative FFT in Figure S5.) Samples with different thicknesses have been measured, and the corresponding round-trip propagation time with respect to the sample thickness is shown in Figure 3b, from which we can extract average longitudinal sound velocities. The obtained sound velocity for pristine MoS_2 is about 3700 m/s. This is slightly higher than the previous first-principles simulation[24] (around 3300 m/s) possibly due to the limited pulse duration in our experiment. In comparison, the longitudinal sound velocity for the CTAB intercalated sample is only 900 m/s. Although we note that these sound velocity values may have limited accuracy, the significant reduction indicates that the longitudinal phonon waves are strongly softened in molecularly inserted samples.

We further performed *ab initio* molecular dynamics simulation to examine the microscopic mechanisms that lead to the drastic changes in vibrational dynamics. The model structure for the intercalated case is built by assuming that CTAB molecules are lying horizontally in the interlayer space. This configuration gives an interlayer spacing that is close to the XRD measurement, thus approximately reproducing the experimental condition. (See the simulation details in the Supporting Information and Figure S6.) First, the drastic changes in the phonon spectrum, observed in the Raman measurement, are confirmed by spectral energy density[36,37] (SED) analysis. SED describes the population of vibrational modes versus frequency based on the temporal Fourier transform of atomic velocities of the MoS_2 lattice. In Figure 4a, we separate the atomic motions in the transverse (x) and vertical (z) directions. SED for pristine MoS_2 exhibits distinct peaks for both directions, corresponding to phonon modes in the center of the Brillouin zone. In contrast, after molecular insertion, well-defined peaks are no longer observed for the transverse direction, and SED instead resembles the phonon density of states of pristine MoS_2 (Figure S6). This indicates that transverse vibrations are strongly disturbed by the molecular interlayer such that the spatial periodicity of the MoS_2 lattice essentially breaks down, consistent with the disappearance of the shearing mode in our Raman measurement. On the other hand, in the vertical direction, we observed a significant softening of the low-frequency interlayer breathing

https://doi.org/10.1021/acs.nanolett.2c01407
Nano Lett. 2022, 22, 5443−5450

mode for intercalated MoS_2. We note that while the breathing mode is generally not observed in Raman measurements due to selection rules,[34] the softening of the breathing mode is consistent with our acoustic measurement showing that the longitudinal sound velocity is significantly reduced.

The breakdown of transverse vibrational modes is a critical contributing factor to the change in the heat conduction behavior. To study its origin, we compare the atomic dynamics of pristine MoS_2 and CTAB-inserted MoS_2. The cross-spectral energy density[38] (cSED) is used to evaluate how atomic motions in different MoS_2 planes are correlated. (See the definition of cSED in the Supporting Information.) Figure 4b compares cSED for transverse atomic motions. Coherent interlayer vibrations will yield cSED close to unity, as found in pristine MoS_2. When vibrations are no longer coherent, atomic motions will be found to be mostly uncorrelated, with cSED close to zero. The small cSED in CTAB-inserted MoS_2 indicates that the vibrational coherence is largely lost. This partial breakdown of vibrational coherence is facilitated by the strong disturbance of molecular vibrations on the MoS_2 lattice. Figure 4c−f further displays the atomic trajectories of Mo and S atoms before and after molecular insertion. It is clear that the trajectories of both Mo and S atoms occupy a significantly larger space, which also implies a higher atomic diffusivity.

Given the above vibrational characterization and molecular dynamics study, we can draw a qualitative picture of the mechanism behind the drastic change in the thermal conductivity. In pristine MoS_2, the cross-plane thermal conductivity is contributed dominantly by acoustic phonons, which include both longitudinal phonons and transverse phonons. After intercalation, the material contains alternating MoS_2 and molecular layers. A simple series thermal resistor picture cannot explain the above results because it would indicate that a larger interlayer distance change should lead to lower thermal conductivity, given that molecules have similar thermal conductivities in their bulk forms. Instead, the lowest thermal conductivity is observed in CTAB-intercalated MoS_2, which has only a modest thickness change. This suggests that the interaction between molecules and the existing MoS_2 lattice strongly affects the atomic vibrations that are responsible for heat transport. The molecular interlayer disturbs the coupling between MoS_2 layers and creates liquid-like atomic motions in the MoS_2 framework. On one hand, this leads to a large reduction in the velocity of longitudinal phonons, thereby reducing their contribution to heat conduction. On the other hand, the transverse phonons are so strongly disturbed that they are no longer well-defined. In fact, because of the molecular interlayer, the periodicity in the cross-plane direction is not strictly obeyed and the material possesses certain disorder. The molecular insertion limits both longitudinal and transverse phonons' contributions to heat transport, thereby largely reducing the material's thermal conductivity.

Finally, we demonstrate that these hybrid materials have the potential to be used as solution-processable coatings for thermal protection. For intercalation in bulk MoS_2 crystals, the interlayer spacing expansion can lead to visible changes in the material thickness (Figure 5a). Molecular insertion with a large spacing expansion (e.g., TDAB intercalation) can further result in the exfoliation of MoS_2 flakes and forms a suspension solution through ultrasonication (Figure 5b). Successful molecular insertion is confirmed by attenuated total reflection Fourier transform infrared (ATR-FTIR) measurements (Figure 5c and Figure S7), showing broadened C−H bonding vibrations compared to the absorption spectrum of the molecules themselves. Solution coating on a substrate further yields multiple flakes with a submicrometer lateral size (Figure 5d).

One advantageous property of these hybrid materials is the intrinsic thermal conductivity anisotropy between the cross-plane and in-plane directions, which can be used to create thermal isolation from the substrate while facilitating lateral heat spreading. We note that an extremely anisotropic MoS_2 thermal conductor was recently reported by rotating MoS_2 interlayers with respect to each other.[39] In our case, molecules will also disturb in-plane thermal transport and thus the anisotropy may not increase after the molecular insertion. Nonetheless, the low cross-plane thermal conductivity is still beneficial for thermal isolation. Conventional methods such as the stacking of heat-conducting and heat-insulating materials can also achieve thermal anisotropy. The advantages of intercalated MoS_2 material include the facts that the thermal anisotropy is intrinsic and the material can be applied down to a thickness scale of hundreds of nanometers. We imagine that these thermal anisotropic materials can be useful in wearable electronic devices, where electronic circuits are often built on polymeric substrates such as PDMS and vertical thermal cross-talk is often undesired, whereas heat spreading is still necessary. As a demonstration, we built a device that resembles the operation of electronic components on soft substrates with local hot spots (Figure 5e). A constant current running through a thin platinum wire sandwiched between two PDMS substrates generates local Joule heating. Without thermal isolation, the heat spreads out uniformly in all directions (Figure 5f). When a thin layer of CTAB-intercalated MoS_2 is placed on the bottom substrate and used as thermal isolation, an elliptical isothermal contour is observed, indicating anisotropic heat transport within the isolation layer. Although we expect that the in-plane heat transport would also be reduced by molecular insertion, the superior heat-insulating property in the cross-plane direction prevents heat from penetrating downward. Consequently, the temperature of the bottom substrate is minimally affected. A transient heating experiment clearly demonstrates that the isolation layer facilitates lateral heat spreading while protecting the substrate from overheating (Supporting Information Movies 2 and 3).

In summary, we have demonstrated that molecular insertion can be quite a general strategy for designing heat insulators. This is rooted in the understanding and control of the vibrational coherence across the entire lattice structure, as revealed by phonon characterization and *ab initio* simulations. The partial breakdown of vibrational coherence also leads to a transition of heat-transport regimes from crystal to glass-like behavior. A nearly 20-fold reduction in the thermal conductivity of CTAB-intercalated MoS_2 is achieved compared to that for pristine samples, which is almost 2 orders of magnitude smaller than for the bulk. These results open up new opportunities for exploring hybrid materials with preferential lattice orientations as heat insulators or thermal switches with a large on/off contrast. We further expect that the optimization of the material properties may create new routes for printable coatings with selective area thermal protection in planar and three-dimensional electronic devices.

https://doi.org/10.1021/acs.nanolett.2c01407
Nano Lett. 2022, 22, 5443−5450

■ ASSOCIATED CONTENT

Supporting Information

The Supporting Information is available free of charge at https://pubs.acs.org/doi/10.1021/acs.nanolett.2c01407.

Details of sample preparation, X-ray diffraction measurements, thermal conductivity measurements, Raman characterization, ab initio molecular dynamics simulations, and infrared microscope measurements (PDF)

In situ observation of the electrochemical intercalation of CTAB in MoS_2 (MP4)

Infrared microscope imaging of lateral heat spreading on a PDMS substrate (MP4)

Infrared microscope imaging of lateral heat spreading on a PDMS substrate with MoS_2-CTAB (MP4)

■ AUTHOR INFORMATION

Corresponding Authors

Harold Y. Hwang − *Department of Applied Physics, Stanford University, Stanford, California 94305, United States; Stanford Institute for Materials and Energy Sciences, SLAC National Accelerator Laboratory, Menlo Park, California 94025, United States*; Email: hyhwang@stanford.edu

Yi Cui − *Department of Materials Science and Engineering, Stanford University, Stanford, California 94305, United States; Stanford Institute for Materials and Energy Sciences, SLAC National Accelerator Laboratory, Menlo Park, California 94025, United States*; orcid.org/0000-0002-6103-6352; Email: yicui@stanford.edu

Authors

Jiawei Zhou − *Department of Materials Science and Engineering, Stanford University, Stanford, California 94305, United States; Stanford Institute for Materials and Energy Sciences, SLAC National Accelerator Laboratory, Menlo Park, California 94025, United States*; orcid.org/0000-0002-9872-5688

Yecun Wu − *Department of Electrical Engineering, Stanford University, Stanford, California 94305, United States; Stanford Institute for Materials and Energy Sciences, SLAC National Accelerator Laboratory, Menlo Park, California 94025, United States*; orcid.org/0000-0001-6011-4489

Heungdong Kwon − *Department of Mechanical Engineering, Stanford University, Stanford, California 94305, United States*; orcid.org/0000-0002-2548-3120

Yanbin Li − *Department of Materials Science and Engineering, Stanford University, Stanford, California 94305, United States; Stanford Institute for Materials and Energy Sciences, SLAC National Accelerator Laboratory, Menlo Park, California 94025, United States*; orcid.org/0000-0002-5285-8602

Xin Xiao − *Department of Materials Science and Engineering, Stanford University, Stanford, California 94305, United States*; orcid.org/0000-0003-1098-9484

Yusheng Ye − *Department of Materials Science and Engineering, Stanford University, Stanford, California 94305, United States; Stanford Institute for Materials and Energy Sciences, SLAC National Accelerator Laboratory, Menlo Park, California 94025, United States*; orcid.org/0000-0001-9832-2478

Yinxing Ma − *Department of Materials Science and Engineering, Stanford University, Stanford, California 94305, United States*

Kenneth E. Goodson − *Department of Mechanical Engineering, Stanford University, Stanford, California 94305, United States*

Complete contact information is available at: https://pubs.acs.org/10.1021/acs.nanolett.2c01407

Author Contributions

[#]J.Z. and Y.W. contributed equally to this work.

Author Contributions

J.Z., Y.W., H.Y.H., and Y.C. conceived the project. J.Z. and H.K. carried out the thermal conductivity measurements. J.Z. performed Raman measurements, picosecond ultrasonic measurements, *ab initio* molecular dynamics simulations, and infrared imaging of the transient heating process. Y.W. and Y.M carried out the sample synthesis and XRD characterization. All authors contributed to the discussion of the results and the writing of the manuscript. All data are available in the main text or the Supporting Information.

Notes

The authors declare no competing financial interest.

■ ACKNOWLEDGMENTS

We thank A. Lindenberg for helpful discussions on the vibrational characterization. This work was supported by the U.S. Department of Energy (DOE), Office of Basic Energy Sciences, Division of Materials Sciences and Engineering (contract no. DE-AC02-76SF00515). Part of this work was performed at the Stanford Nano Shared Facilities (SNSF), supported by the National Science Foundation under award ECCS-1542152.

■ REFERENCES

(1) Qian, X.; Zhou, J.; Chen, G. Phonon-engineered extreme thermal conductivity materials. *Nat. Mater.* **2021**, *20*, 1188−1202.

(2) Moore, A. L.; Shi, L. Emerging challenges and materials for thermal management of electronics. *Mater. Today* **2014**, *17*, 163−174.

(3) Lindsay, L.; Broido, D. A.; Reinecke, T. L. First-principles determination of ultrahigh thermal conductivity of boron arsenide: A competitor for diamond? *Phys. Rev. Lett.* **2013**, *111*, 025901.

(4) Feng, T.; Lindsay, L.; Ruan, X. Four-phonon scattering significantly reduces intrinsic thermal conductivity of solids. *Phys. Rev. B* **2017**, *96*, 161201.

(5) Tian, F.; et al. Unusual high thermal conductivity in boron arsenide bulk crystals. *Science* **2018**, *361*, 582−585.

(6) Li, S.; et al. High thermal conductivity in cubic boron arsenide crystals. *Science* **2018**, *361*, 579−581.

(7) Kang, J. S.; Li, M.; Wu, H.; Nguyen, H.; Hu, Y. Experimental observation of high thermal conductivity in boron arsenide. *Science* **2018**, *361*, 575−578.

(8) Chen, K.; et al. Ultrahigh thermal conductivity in isotope-enriched cubic boron nitride. *Science* **2020**, *367*, 555−559.

(9) Peierls, R. Zur kinetischen theorie der wärmeleitung in kristallen. *Ann. Phys.* **1929**, *395*, 1055−1101.

(10) Biswas, K.; et al. High-performance bulk thermoelectrics with all-scale hierarchical architectures. *Nature* **2012**, *489*, 414−418.

(11) Chiritescu, C.; et al. Ultralow thermal conductivity in disordered, layered WSe_2 crystals. *Science* **2007**, *315*, 351−353.

(12) Chen, G. Non-Fourier phonon heat conduction at the microscale and nanoscale. *Nat. Rev. Phys.* **2021**, *3*, 555−569.

(13) Luckyanova, M. N.; et al. Phonon localization in heat conduction. *Sci. Adv.* **2018**, *4*, eaat9460.

(14) Mukhopadhyay, S.; et al. Two-channel model for ultralow thermal conductivity of crystalline Tl_3VSe_4. *Science* **2018**, *360*, 1455−1458.

(15) Gibson, Q. D.; et al. Low thermal conductivity in a modular inorganic material with bonding anisotropy and mismatch. *Science* **2021**, *373*, 1017−1022.
(16) Pisoni, A.; et al. Ultra-low thermal conductivity in organic−inorganic hybrid perovskite $CH_3NH_3PbI_3$. *J. Phys. Chem. Lett.* **2014**, *5*, 2488−2492.
(17) Li, B.; et al. Polar rotor scattering as atomic-level origin of low mobility and thermal conductivity of perovskite $CH_3NH_3PbI_3$. *Nat. Commun.* **2017**, *8*, 16086.
(18) Niedziela, J. L.; et al. Selective breakdown of phonon quasiparticles across superionic transition in $CuCrSe_2$. *Nat. Phys.* **2019**, *15*, 73−78.
(19) Liu, H.; et al. Copper ion liquid-like thermoelectrics. *Nat. Mater.* **2012**, *11*, 422−425.
(20) Minnich, A. J. Phonon heat conduction in layered anisotropic crystals. *Phys. Rev. B* **2015**, *91*, 085206.
(21) Cho, J.; et al. Electrochemically tunable thermal conductivity of lithium cobalt oxide. *Nat. Commun.* **2014**, *5*, 4035.
(22) Sood, A.; et al. An electrochemical thermal transistor. *Nat. Commun.* **2018**, *9*, 4510.
(23) Zhu, G.; et al. Tuning thermal conductivity in molybdenum disulfide by electrochemical intercalation. *Nat. Commun.* **2016**, *7*, 13211.
(24) Gu, X.; Li, B.; Yang, R. Layer thickness-dependent phonon properties and thermal conductivity of MoS_2. *J. Appl. Phys.* **2016**, *119*, 085106.
(25) Wang, C.; et al. Monolayer atomic crystal molecular superlattices. *Nature* **2018**, *555*, 231−236.
(26) Cahill, D. G. Analysis of heat flow in layered structures for time-domain thermoreflectance. *Rev. Sci. Instrum.* **2004**, *75*, 5119.
(27) Schmidt, A. J.; Chen, X.; Chen, G. Pulse accumulation, radial heat conduction, and anisotropic thermal conductivity in pump-probe transient thermoreflectance. *Rev. Sci. Instrum.* **2008**, *79*, 114902.
(28) Sood, A.; et al. Quasi-ballistic thermal transport across MoS_2 thin films. *Nano Lett.* **2019**, *19*, 2434−2442.
(29) Losego, M. D.; Blitz, I. P.; Vaia, R. A.; Cahill, D. G.; Braun, P. V. Ultralow thermal conductivity in organoclay nanolaminates synthesized via simple self-assembly. *Nano Lett.* **2013**, *13*, 2215−2219.
(30) Uma, S.; McConnell, A. D.; Asheghi, M.; Kurabayashi, K.; Goodson, K. E. Temperature-dependent thermal conductivity of undoped polycrystalline silicon layers. *Int. J. Thermophys.* **2001**, *22*, 605−616.
(31) Sheng, P.; Zhou, M. Heat conductivity of amorphous solids: Simulation results on model structures. *Science* **1991**, *253*, 539−542.
(32) Allen, P. B.; Feldman, J. L.; Fabian, J.; Wooten, F. Diffusons, locons and propagons: Character of atomie yibrations in amorphous Si. *Philos. Mag. B* **1999**, *79*, 1715−1731.
(33) Shulumba, N.; Hellman, O.; Minnich, A. J. Lattice thermal conductivity of polyethylene molecular crystals from first-principles including nuclear quantum effects. *Phys. Rev. Lett.* **2017**, *119*, 185901.
(34) Zhang, X.; et al. Phonon and Raman scattering of two-dimensional transition metal dichalcogenides from monolayer, multilayer to bulk material. *Chem. Soc. Rev.* **2015**, *44*, 2757−2785.
(35) Carvalho, B. R.; et al. Intervalley scattering by acoustic phonons in two-dimensional MoS_2 revealed by double-resonance Raman spectroscopy. *Nat. Commun.* **2017**, *8*, 14670.
(36) Thomas, J. A.; Turney, J. E.; Iutzi, R. M.; Amon, C. H.; McGaughey, A. J. H. Predicting phonon dispersion relations and lifetimes from the spectral energy density. *Phys. Rev. B* **2010**, *81*, 081411.
(37) De Koker, N. Thermal conductivity of MgO periclase from equilibrium first principles molecular dynamics. *Phys. Rev. Lett.* **2009**, *103*, 125902.
(38) Latour, B.; Chalopin, Y. Distinguishing between spatial coherence and temporal coherence of phonons. *Phys. Rev. B* **2017**, *95*, 214310.
(39) Kim, S. E.; et al. Extremely anisotropic van der Waals thermal conductors. *Nature* **2021**, *597*, 660−665.

https://doi.org/10.1021/acs.nanolett.2c01407
Nano Lett. 2022, 22, 5443−5450